

Magnetotransport in the presence of real and momentum space topology

Azaz Ahmad^{1,2,3} and Takami Tohyama³

¹*Department of Physics, Indian Institute of Technology, Kanpur-208016, India.*

²*School of Physical Sciences, Indian Institute of Technology Mandi, Mandi 175005, India.*

³*Department of Applied Physics, Tokyo University of Science, Katsushika, Tokyo 125-8585, Japan.*
(Dated: March 16, 2026)

We investigate magnetotransport in a time-reversal symmetry–broken, untilted Weyl semimetal in the simultaneous presence of momentum-space Berry curvature and real-space topology arising from a skyrmion-induced emergent magnetic field \mathbf{B}_{emer} . Using a semiclassical Boltzmann approach incorporating Berry-curvature corrections and intervalley scattering, we analyze the longitudinal magnetoconductivity and planar Hall conductivity in this mixed-topology regime. In the absence of B_{emer} , increasing intervalley scattering drives a strong sign reversal of the longitudinal magnetoconductivity. A finite \mathbf{B}_{emer} introduces an additional shift of the parabolic magnetic-field dependence, leading to a weak sign-reversal regime without altering the curvature. The coexistence of these effects naturally produces a strong-and-weak sign-reversal regime, demonstrating that intervalley scattering and real-space topology control distinct geometric features of the response. The emergent field further induces asymmetry in the angular dependence of both longitudinal and planar Hall conductivities. We show that a finite planar Hall response can arise solely from \mathbf{B}_{emer} when its direction is varied, providing a transport signature of real-space topology. Our results establish that the skyrmion-induced emergent field acts as an independent topological tuning parameter, revealing measurable consequences of the interplay between real- and momentum-space Berry curvature in Weyl systems.

I. INTRODUCTION

Topological semimetals realized in kagome-lattice materials provide a natural platform in which distinct forms of topology can coexist and mutually influence electronic transport [1–4]. In Weyl semimetals (WSMs), momentum \mathbf{k} -space topology arises from isolated band-touching points (Weyl nodes) that act as monopoles of Berry curvature $\Omega_{\mathbf{k}}^{\chi}$ with chirality $\chi = \pm 1$ [5, 6]. The associated Berry curvature profoundly modifies semiclassical transport, generating anomalous velocity contributions and phase-space corrections that underlie phenomena such as the anomalous Hall effect and the chiral anomaly [7, 8]. These effects are now well established in Weyl systems [9–14].

Kagome-lattice materials, however, offer an additional ingredient: nontrivial real-space spin textures. Owing to geometrical frustration, strong spin–orbit coupling, and magnetic ordering tendencies, kagome systems can host complex magnetic configurations including noncoplanar spin states and skyrmion textures [15–17]. When the electronic spins adiabatically follow such a smoothly varying magnetization texture $\mathbf{n}(\mathbf{r})$, they acquire a real-space Berry phase that manifests as an emergent magnetic field $\mathbf{B}_{\text{emer}} = \frac{\hbar}{2e} \mathbf{n} \cdot (\partial_x \mathbf{n} \times \partial_y \mathbf{n}) \hat{e}$, where \hat{e} is the unit vector pointing in the direction of the field. \mathbf{B}_{emer} acts on the charge carriers analogously to an external magnetic field \mathbf{B} [12]. This mechanism is responsible for the topological Hall effect in chiral magnets and has been widely discussed in systems with noncoplanar spin order [12, 18–20].

In a kagome WSM hosting both Weyl nodes and a nontrivial magnetic texture, electrons therefore experience two distinct topological fields: the Berry

curvature in momentum space and the emergent magnetic field in real space [1–4]. Within the semiclassical Boltzmann framework, the equations of motion depend only on the total magnetic field $\mathbf{B}_{\text{tot}} = \mathbf{B} + \mathbf{B}_{\text{emer}}$. As a result, the modified phase-space factor that controls the dynamics of the electrons becomes $\mathcal{D}^{\chi} = (1 + \frac{e}{\hbar} \mathbf{B}_{\text{tot}} \cdot \Omega_{\mathbf{k}}^{\chi})^{-1}$ [7, 21]. This expression explicitly contains the cross term $\mathbf{B}_{\text{emer}} \cdot \Omega_{\mathbf{k}}^{\chi}$, which encodes the interplay between real-space and momentum-space topology. Importantly, the intrinsic Berry curvature of the Weyl nodes remains unchanged; rather, it is the emergent field that modifies the effective magnetic environment in which the Weyl quasiparticles propagate. Consequently, magnetotransport in such systems carries signatures of a mixed real–momentum topological response. In particular, longitudinal magnetoconductivity (LMC) and PHC (PHC) acquire corrections controlled by \mathbf{B}_{emer} , allowing magnetic texture effects to directly influence anomaly-driven transport. Kagome Weyl materials therefore provide an experimentally relevant setting in which this real–momentum topological mixing can be probed through standard magnetotransport measurements. A central conceptual advance of this work is the identification of a *mixed topological magnetotransport mechanism* arising from the interplay between real-space and momentum-space topology. While previous studies have focused on strain-induced axial fields that are introduced as chirality-dependent gauge fields by construction [14, 22–26], here the chirality dependence of the transport response emerges *dynamically* from the coupling between the real-space emergent field and the intrinsic Berry curvature of Weyl fermions.

In our framework, although \mathbf{B}_{emer} is identical for both Weyl nodes, its projection onto the Berry curvature $\mathbf{B}_{\text{emer}} \cdot \boldsymbol{\Omega}_{\mathbf{k}}^{\chi}$ automatically acquires opposite signs for opposite chiralities due to $\boldsymbol{\Omega}_{\mathbf{k}}^{\chi} \propto \chi$ [21]. The resulting transport corrections, therefore, mimic axial-field-like magnetotransport without invoking any explicit chiral gauge field. This demonstrates that axial-type longitudinal and planar Hall responses can arise purely from the coexistence of momentum-space monopoles and real-space skyrmion topology. Our results thus establish a direct bridge between two distinct topological structures: the Weyl monopole in momentum space and the skyrmion winding number in real space. The magnetotransport response can be interpreted as a mixed topological coupling proportional to the product of these two topological charges, providing a unified description of anomaly-like transport phenomena driven by magnetic texture topology.

The remainder of the paper is organized as follows. In Sec. II, we introduce the minimal model of a time-reversal symmetry-broken WSM and Sec. III outline the semiclassical Boltzmann formalism incorporating Berry-curvature corrections and the emergent magnetic field arising from real-space topology. In Sec. IV, we classify different regimes of sign reversal and present detailed results for the LMC and PHC in the presence of mixed real- and momentum-space topology. Finally, in Sec. V, we summarize our main findings and discuss their physical implications.

II. LOW-ENERGY MODEL FOR MIXED REAL- AND MOMENTUM-SPACE TOPOLOGY

To investigate transport arising from the interplay of momentum-space and real-space topology, we begin with the minimal low-energy Hamiltonian describing quasiparticles near a pair of Weyl nodes. In the absence of magnetic texture, the effective Hamiltonian reads [6, 27–29]:

$$H_{\text{WSM}}^{\chi}(\mathbf{k}) = \chi \hbar v_{\text{F}} \mathbf{k} \cdot \boldsymbol{\sigma}, \quad (1)$$

where $\chi = \pm 1$ denotes the chirality (topological charge) of the Weyl node, v_{F} is the Fermi velocity, and $\boldsymbol{\sigma}$ represents the Pauli matrices acting in pseudospin space. The wave vector \mathbf{k} is measured from the Weyl node. For clarity and to isolate the essential mixed-topological contribution, we restrict our analysis to a single pair of Weyl cones, noting that additional pairs modify only the total response quantitatively [21, 30]. Diagonalization of Eq. (1) yields the linear dispersion

$$\epsilon_{\mathbf{k}} = \pm \hbar v_{\text{F}} |\mathbf{k}|. \quad (2)$$

The orbital magnetic moment (OMM), arising from the self-rotation of the Bloch wave packet, plays an important role in the semiclassical dynamics. It is given

by [11]:

$$\begin{aligned} \mathbf{m}_{\mathbf{k}}^{\chi} &= -\frac{ie}{2\hbar} \text{Im} \left\langle \nabla_{\mathbf{k}} u^{\chi}(\mathbf{k}) \left[\left[\epsilon_{\mathbf{k}} - \hat{H}_{\text{WSM}}^{\chi}(\mathbf{k}) \right] \nabla_{\mathbf{k}} u^{\chi}(\mathbf{k}) \right] \right\rangle \\ &\equiv -\chi e v_{\text{F}} \mathbf{k} / 2k^2, \end{aligned} \quad (3)$$

where $u^{\chi}(\mathbf{k})$ is the Bloch wave packet in the WSM. The coupling of the OMM to a total magnetic field \mathbf{B}_{tot} modifies the band dispersion according to $\epsilon_{\mathbf{k}}^{\chi} = \epsilon_{\mathbf{k}} - \mathbf{m}_{\mathbf{k}}^{\chi} \cdot \mathbf{B}_{\text{tot}}$. Consequently, the constant-energy contour at the Fermi energy ϵ_{F} is obtained as [21, 31, 32]:

$$k_{\text{F}}^{\chi} = \frac{\epsilon_{\text{F}} + \sqrt{\epsilon_{\text{F}}^2 - n\chi e v_{\text{F}} B_{\text{tot}} \beta_{\theta\phi}}}{n}, \quad (4)$$

where $n = 2\hbar v_{\text{F}}$. By using θ and ϕ as polar and azimuthal angles of the Bloch eigenvectors, respectively (see below), the geometric factor $\beta_{\theta\phi}$ is given by

$$\begin{aligned} \beta_{\theta\phi} &= \sin \theta \cos \phi (\cos \gamma + \cos \gamma_{\text{emer}}) \\ &\quad + \cos \theta (\sin \gamma + \sin \gamma_{\text{emer}}), \end{aligned} \quad (5)$$

where the direction of the magnetic fields is assumed in the xz plane, measured with respect to the \hat{x} -axis, i.e., $\mathbf{B} = B(\cos \gamma, 0, \sin \gamma)$ and $\mathbf{B}_{\text{emer}} = B_{\text{emer}}(\cos \gamma_{\text{emer}}, 0, \sin \gamma_{\text{emer}})$. The nontrivial topology of the Weyl node is encoded in its Bloch eigenvectors,

$$|u^{+}\rangle^T = [e^{-i\phi} \cos(\theta/2), \sin(\theta/2)], \quad (6)$$

$$|u^{-}\rangle^T = [-e^{-i\phi} \sin(\theta/2), \cos(\theta/2)], \quad (7)$$

which generate a singular Berry curvature in momentum space,

$$\boldsymbol{\Omega}_{\mathbf{k}}^{\chi} = i \nabla_{\mathbf{k}} \times \langle u^{\chi}(\mathbf{k}) | \nabla_{\mathbf{k}} | u^{\chi}(\mathbf{k}) \rangle \equiv -\chi \frac{\mathbf{k}}{2k^3}, \quad (8)$$

acting as a monopole of Berry flux located at the Weyl node [7, 11]. This momentum-space Berry curvature underlies anomalous transport responses such as the anomalous Hall effect and chiral-anomaly-induced magnetotransport [21, 30–54].

When the WSM hosts a slowly varying magnetic texture $\mathbf{n}(\mathbf{r})$, such as a skyrmion lattice, electrons traversing the texture acquire an additional real-space Berry phase. In the adiabatic regime where the magnetic texture varies on a length scale much larger than the electronic wavelength, the effect of the texture can be captured through an emergent magnetic field [12, 55], $\mathbf{B}_{\text{emer}} = \frac{\hbar}{2e} \mathbf{n} \cdot (\partial_x \mathbf{n} \times \partial_y \mathbf{n}) \hat{e}$, which is directly proportional to the skyrmion density. Unlike the external magnetic field, \mathbf{B}_{emer} originates purely from real-space topology and exists even in the absence of applied fields. In systems where Weyl band topology coexists with skyrmion textures, as realized in magnetic kagome materials and related chiral magnets [1–4], charge carriers therefore experience *two independent sources of Berry curvature*: (i) Momentum-space Berry curvature

$\Omega_{\mathbf{k}}^{\chi}$ associated with Weyl nodes, and (ii) Real-space Berry curvature encoded in \mathbf{B}_{emer} . Within the semiclassical description, both fields enter the equations of motion through the modified phase-space factor

$$\mathcal{D}^{\chi} = \left[1 + \frac{e}{\hbar} (\mathbf{B} + \mathbf{B}_{\text{emer}}) \cdot \Omega_{\mathbf{k}}^{\chi} \right]^{-1}. \quad (9)$$

The crucial new ingredient is the mixed scalar product $\mathbf{B}_{\text{emer}} \cdot \Omega_{\mathbf{k}}^{\chi}$, which vanishes unless both real-space and momentum-space topology are simultaneously present. This term modifies the density of states and transport coefficients, giving rise to additional contributions to LMC and PHC that are absent in ordinary metals and in systems hosting only one type of topology. Thus, the effective low-energy model of Eq. (1), supplemented by the emergent field \mathbf{B}_{emer} , provides the minimal theoretical framework required to describe *mixed real-momentum space topological transport*.

We assume that the length scale of the skyrmion textures is much smaller than the length of the system, so that the charge carrier experiences an average, uniform \mathbf{B}_{emer} . This leads to the momentum-dependent but position-independent phase-space factor $\mathcal{D}_{\mathbf{k}}^{\chi}$. The magnitude of the emergent magnetic field generated by a skyrmion texture is determined by the skyrmion density through $B_{\text{emer}} = n_{\text{sk}} \Phi_0$, where $\Phi_0 = h/e$ is the flux quantum. For typical skyrmion sizes of ~ 50 – 100 nm observed in chiral magnets, the corresponding emergent magnetic field lies in the range 10^{-2} – 1 T. Therefore, the parameter range $B_{\text{emer}} = 0$ – 0.25 T used in our calculations falls well within experimentally realistic values.

III. MAXWELL BOLTZMANN TRANSPORT FORMALISM FOR ELECTRON TRANSPORT IN SKYRMION

Using the quasiclassical Boltzmann transport theory, we study transport in WSMs in the limit of weak electric and magnetic fields. Since the quasiclassical Boltzmann theory is valid when the chemical potential μ is away from the nodal point such that $\mu^2 \gg \hbar v_{\text{F}}^2 e |\mathbf{B}_{\text{tot}}|$, we assume that μ lies in the conduction band without loss of generality. The phenomenological Boltzmann equation for the non-equilibrium distribution function $f_{\mathbf{k}}^{\chi}$ can be expressed as [40, 56–60]

$$\left(\frac{\partial}{\partial t} + \dot{\mathbf{r}}^{\chi} \cdot \nabla_{\mathbf{r}} + \dot{\mathbf{k}}^{\chi} \cdot \nabla_{\mathbf{k}} \right) f_{\mathbf{k}}^{\chi} = \mathcal{I}_{\text{coll}}[f_{\mathbf{k}}^{\chi}], \quad (10)$$

where the collision term $\mathcal{I}_{\text{coll}}$ incorporates impurity scattering. In the presence of an external magnetic field \mathbf{B} , a real-space emergent magnetic field \mathbf{B}_{emer} , and an electric field \mathbf{E} , the semiclassical equations of motion

become [7, 10, 11, 57, 61]

$$\begin{aligned} \dot{\mathbf{r}}^{\chi} &= \mathcal{D}_{\mathbf{k}}^{\chi} \left[\mathbf{v}_{\mathbf{k}}^{\chi} + \frac{e}{\hbar} \mathbf{E} \times \Omega_{\mathbf{k}}^{\chi} + \frac{e}{\hbar} (\mathbf{v}_{\mathbf{k}}^{\chi} \cdot \Omega_{\mathbf{k}}^{\chi}) \mathbf{B}_{\text{tot}} \right], \\ \dot{\mathbf{k}}^{\chi} &= -\frac{e}{\hbar} \mathcal{D}_{\mathbf{k}}^{\chi} \left[\mathbf{E} + \mathbf{v}_{\mathbf{k}}^{\chi} \times \mathbf{B}_{\text{tot}} + \frac{e}{\hbar} (\mathbf{E} \cdot \mathbf{B}_{\text{tot}}) \Omega_{\mathbf{k}}^{\chi} \right], \end{aligned} \quad (11)$$

where $\mathbf{v}_{\mathbf{k}}^{\chi}$ is the band velocity calculated using $\epsilon_{\mathbf{k}}^{\chi}$. The collision integral includes both intra-node and inter-node scattering [30, 57, 62–64]:

$$\mathcal{I}_{\text{coll}}[f_{\mathbf{k}}^{\chi}] = \sum_{\chi'} \sum_{\mathbf{k}'} W_{\mathbf{k}\mathbf{k}'}^{\chi\chi'} (f_{\mathbf{k}'}^{\chi'} - f_{\mathbf{k}}^{\chi}) \quad (12)$$

with scattering rate calculated using Fermi's golden rule [62–65],

$$W_{\mathbf{k}\mathbf{k}'}^{\chi\chi'} = \frac{2\pi}{\hbar} \frac{n_i}{\mathcal{V}} |\langle u^{\chi'}(\mathbf{k}') | U_{\mathbf{k}\mathbf{k}'}^{\chi\chi'} | u^{\chi}(\mathbf{k}) \rangle|^2 \delta(\epsilon_{\mathbf{k}'}^{\chi'} - \epsilon_{\mathbf{k}}^{\chi}), \quad (13)$$

where n_i is the concentration of impurities, \mathcal{V} is the volume of the system, and $U_{\mathbf{k}\mathbf{k}'}^{\chi\chi'}$ is the profile of the scattering potential. Assuming non-magnetic point-like impurities with momentum-independent and chirality-dependent amplitudes, i.e. $U_{\mathbf{k}\mathbf{k}'}^{\chi\chi'} = U^{\chi\chi'}$, we can express the square of the matrix elements as $\mathcal{G}^{\chi\chi'} \equiv |\langle u^{\chi'}(\mathbf{k}') | U_{\mathbf{k}\mathbf{k}'}^{\chi\chi'} | u^{\chi}(\mathbf{k}) \rangle|^2 = |U^{\chi\chi'}|^2 \mathcal{V}^2 [1 + \chi\chi' (\cos\theta \cos\theta' + \sin\theta \sin\theta' \cos\phi \cos\phi' + \sin\theta \sin\theta' \sin\phi \sin\phi')]$. Here, it is worth highlighting that, in our formalism, the relative strength of the intra- and inter-node scattering channels can be tuned using the parameter defined as:

$$\alpha = \frac{U^{\chi\chi'}}{U^{\chi\chi}} \quad (\chi' \neq \chi). \quad (14)$$

Fixing $\mathbf{E} = E\hat{z}$, we expand $f_{\mathbf{k}}^{\chi}$ in terms of E as $f_{\mathbf{k}}^{\chi} = f_0 + g_{\mathbf{k}}^{\chi}$ with the Fermi distribution function f_0 and $g_{\mathbf{k}}^{\chi} = e \left(-\frac{\partial f_0}{\partial \epsilon_{\mathbf{k}}^{\chi}} \right) E \Lambda_{\mathbf{k}}^{\chi}$, where $\Lambda_{\mathbf{k}}^{\chi}$ represents the z -component of unknown function (ansatz) to be evaluated [42, 51, 66, 67]. Keeping terms linear in \mathbf{E} , the Boltzmann equation becomes [31, 57, 63, 64, 67, 68]:

$$\begin{aligned} \mathcal{D}_{\mathbf{k}}^{\chi} \left[v_{\mathbf{k}}^{\chi z} + \frac{e(B \sin\gamma + B_{\text{emer}} \sin\gamma_{\text{emer}})}{\hbar} (\Omega_{\mathbf{k}}^{\chi} \cdot \mathbf{v}_{\mathbf{k}}^{\chi}) \right] \\ = \sum_{\chi'} \sum_{\mathbf{k}'} W_{\mathbf{k}\mathbf{k}'}^{\chi'\chi} (\Lambda_{\mathbf{k}'}^{\chi'} - \Lambda_{\mathbf{k}}^{\chi}). \end{aligned} \quad (15)$$

Here, we define the band scattering rate as

$$\frac{1}{\tau_{\mathbf{k}}^{\chi}(\theta, \phi)} = \sum_{\chi'} \mathcal{V} \int \frac{d^3\mathbf{k}'}{(2\pi)^3} (\mathcal{D}_{\mathbf{k}'}^{\chi'})^{-1} W_{\mathbf{k}\mathbf{k}'}^{\chi\chi'}. \quad (16)$$

Using Eq. (16), we can write Eq. (15) as

$$h_{\mathbf{k}}^{\chi}(\theta, \phi) + \frac{\Lambda_{\mathbf{k}}^{\chi}(\theta, \phi)}{\tau_{\mathbf{k}}^{\chi}(\theta, \phi)} \quad (17)$$

$$= \nu \sum_{\chi'} \int \frac{d^3 \mathbf{k}'}{(2\pi)^3} (\mathcal{D}_{\mathbf{k}'}^{\chi'})^{-1} W_{\mathbf{k}\mathbf{k}'}^{\chi\chi'} \Lambda_{\mathbf{k}'}^{\chi'}(\theta', \phi'). \quad (18)$$

Here, $h_{\mathbf{k}}^{\chi}(\theta, \phi) = \mathcal{D}_{\mathbf{k}}^{\chi} [v_{z,\mathbf{k}}^{\chi} + \frac{eB \sin \gamma + B_{\text{emer}} \sin \gamma_{\text{emer}}}{\hbar} (\boldsymbol{\Omega}_{\mathbf{k}}^{\chi} \cdot \mathbf{v}_{\mathbf{k}}^{\chi})]$ and is evaluated at the Fermi energy. In the low temperature limit, for a constant Fermi energy surface, Eq. (16) and the right-hand side of Eq. (18) are reduced to integration over θ' and ϕ' ,

$$\begin{aligned} \frac{1}{\tau_{\mathbf{k}}^{\chi}(\theta, \phi)} &= \nu \sum_{\chi'} \Pi^{\chi\chi'} \\ &\times \iint \frac{(k_{\text{F}}^{\chi'})^3 \sin \theta'}{|\mathbf{v}_{\mathbf{k}'_{\text{F}}}^{\chi'} \cdot \mathbf{k}'_{\text{F}}|} d\theta' d\phi' \mathcal{G}^{\chi\chi'} (\mathcal{D}_{\mathbf{k}'}^{\chi'})^{-1} \\ &= \nu \sum_{\chi'} \Pi^{\chi\chi'} \iint f^{\chi'}(\theta', \phi') \mathcal{G}^{\chi\chi'} \Lambda_{\mathbf{k}}^{\chi'} / \tau_{\mathbf{k}}^{\chi} d\theta' d\phi', \quad (19) \end{aligned}$$

where $\Pi^{\chi\chi'} = n_i / 4\pi^2 \hbar^2$ and $f^{\chi}(\theta, \phi) = \frac{(k_{\text{F}}^{\chi})^3}{|\mathbf{v}_{\mathbf{k}'_{\text{F}}}^{\chi} \cdot \mathbf{k}'_{\text{F}}|} \sin \theta (\mathcal{D}_{\mathbf{k}}^{\chi})^{-1} \tau_{\mathbf{k}}^{\chi}(\theta, \phi)$. Using ansatz $\Lambda_{\mathbf{k}}^{1,\chi} = (d^{\chi} - h_{\mathbf{k}}^{\chi} + a^{\chi} \cos \theta + b^{\chi} \sin \theta \cos \phi + c^{\chi} \sin \theta \sin \phi) \tau_{\mathbf{k}}^{\chi}(\theta, \phi)$, Eq. (19) can be written in the following form:

$$\begin{aligned} &d^{\chi} + a^{\chi} \cos \theta + b^{\chi} \sin \theta \cos \phi + c^{\chi} \sin \theta \sin \phi \\ &= \sum_{\chi'} \Pi^{\chi\chi'} \iint f^{\chi'}(\theta', \phi') \mathcal{G}^{\chi\chi'} d\theta' d\phi' \\ &\times (d^{\chi} - h_{\mathbf{k}}^{\chi} + a^{\chi} \cos \theta + b^{\chi} \sin \theta \cos \phi + c^{\chi} \sin \theta \sin \phi). \quad (20) \end{aligned}$$

When the aforementioned equation is explicitly stated, it appears as seven simultaneous equations that must be solved for eight variables. The conservation of particle numbers provides an additional restriction:

$$\sum_{\chi} \sum_{\mathbf{k}} g_{\mathbf{k}}^{\chi} = 0. \quad (21)$$

For eight unknown variables $(d^{\pm 1}, a^{\pm 1}, b^{\pm 1}, c^{\pm 1})$, Eqs. (20) and (21) are simultaneously solved with Eq. (19). Due to the intricate structure of the equations, all two-dimensional integrals with respect to θ' and ϕ' are carried out numerically and the solution of simultaneous equations are obtained.

Once the distribution function $f_{\mathbf{k}}^{\chi}$ is evaluated, the current density can be evaluated as:

$$\mathbf{J} = -e \sum_{\chi, \mathbf{k}} f_{\mathbf{k}}^{\chi} \dot{\mathbf{r}}^{\chi}. \quad (22)$$

The generalized velocity $\dot{\mathbf{r}}_{\mathbf{k}}^{\chi}$ can be written as $\dot{\mathbf{r}}^{\chi} = \mathbf{v}_0^{\chi} + \mathbf{v}_1^{\chi}$, where \mathbf{v}_0^{χ} and \mathbf{v}_1^{χ} correspond to the velocities without

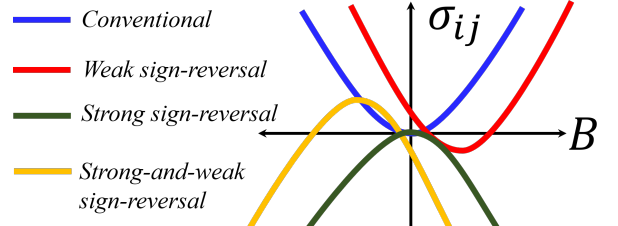


Figure 1. A schematic illustration of the characteristic regimes of magnetoconductivity σ_{ij} in WSMs in the presence of both external magnetic field B and emergent field B_{emer} . The figure highlights *weak sign reversal* (shifted parabola), *strong sign reversal* (curvature inversion), and the coexisting *strong-and-weak sign-reversal* regime, in contrast to the conventional quadratic-in- B response. In the present mixed-topology setting, these regimes arise from the interplay between intervalley scattering and the real-space Berry-curvature contribution encoded in B_{emer} [22, 32, 69].

and with the electric field, respectively. The Explicit expressions are

$$\begin{aligned} \mathbf{v}_0^{\chi} &= \left(\frac{e\mathcal{D}_{\mathbf{k}}^{\chi}}{\hbar} \right) \left(\mathbf{v}_{\mathbf{k}}^{\chi} \cdot \boldsymbol{\Omega}_{\mathbf{k}}^{\chi} \mathbf{B}_{\text{tot}} + \frac{\hbar}{e} \mathbf{v}_{\mathbf{k}}^{\chi} \right), \quad (23) \\ \mathbf{v}_1^{\chi} &= \left(\frac{e\mathcal{D}_{\mathbf{k}}^{\chi}}{\hbar} \right) (\mathbf{E} \times \boldsymbol{\Omega}_{\mathbf{k}}^{\chi}). \end{aligned}$$

Now, from Eq. (22), the generalized current response is given by

$$\mathbf{J} = -e \sum_{\chi, \mathbf{k}} (\mathbf{v}_0^{\chi} f_0^{\chi} + \mathbf{v}_1^{\chi} f_0^{\chi} + \mathbf{v}_0^{\chi} g_{\mathbf{k}}^{\chi}). \quad (24)$$

In the next sections, we evaluate LMC, σ_{zz} , and PHC, σ_{xz} , defined as $J_z = \sigma_{zz} E$ and $J_x = \sigma_{xz} E$, respectively. Unless otherwise stated, we use the following parameter values: Fermi velocity $v_{\text{F}} = 10^6$ m/s and Fermi energy $\epsilon_{\text{F}} = 0.05$ eV.

IV. RESULTS AND DISCUSSIONS

Before presenting the detailed numerical results, we first clarify the classification of different types of sign reversal of LMC in the present mixed-topology setting. The sign of LMC in WSMs has been extensively investigated in earlier works [31, 57, 70]. In an untilted WSM, the chiral anomaly typically produces a positive LMC under weak intervalley scattering; however, when intervalley scattering becomes sufficiently strong, the LMC undergoes a sign reversal. This mechanism originates from the competition between anomaly-driven charge pumping and relaxation processes.

In the present work, an additional ingredient enters the problem to enrich the dynamics of the electrons: the emergent magnetic field \mathbf{B}_{emer} , which represents

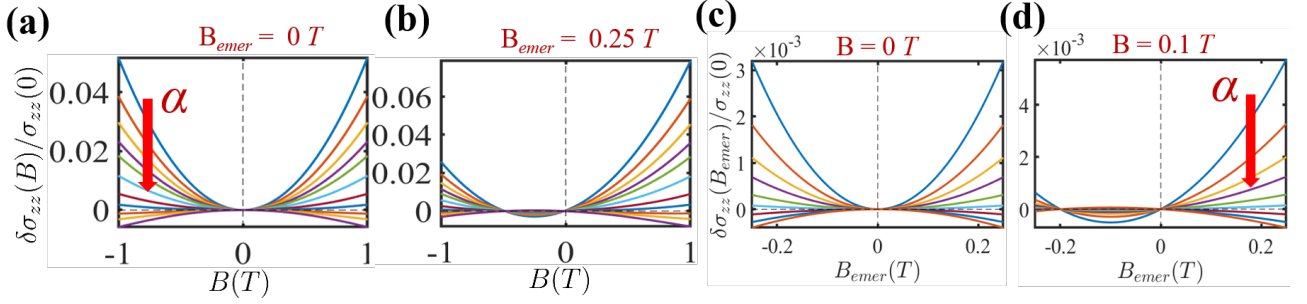


Figure 2. Normalized LMC for a minimal model of a time-reversal symmetry broken, untitled WSM in the presence of an emergent magnetic field \mathbf{B}_{emer} arising from real-space topology. The angle of \mathbf{B}_{emer} and an external magnetic field \mathbf{B} is set to be $\gamma_{\text{emer}} = \gamma = \pi/2$. In all the panels, α varies from 0.20 to 1.50 along the red arrow. (a) $B_{\text{emer}} = 0$ T and changing B . At $\alpha_c \simeq 0.80$, the anomaly-driven sign change of LMC occurs [33]. (b) $B_{\text{emer}} = 0.25$ T and changing B . For $\alpha < \alpha_c$ ($\alpha > \alpha_c$), weak sign-reversal (strong-and-weak sign-reversal) behaviors emerge. (c) $B = 0$ T and changing B_{emer} . The sign change occurs at α_c . (d) $B = 0.1$ T and changing B_{emer} .

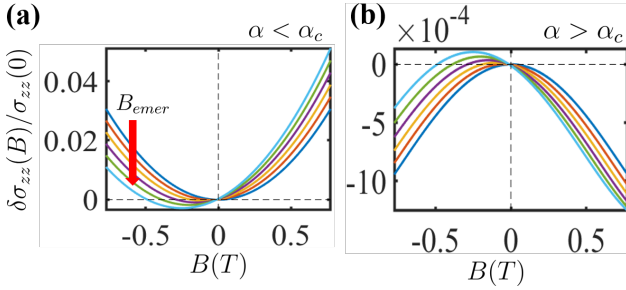


Figure 3. Normalized LMC as a function of the external magnetic field \mathbf{B} with $\gamma = \pi/2$ for a minimal model of an untitled time-reversal symmetry broken WSM. (a) Weak sing-reversal regime ($\alpha = 0.2 < \alpha_c \simeq 0.80$) and (b) strong-and-weak sing-reversal regime ($\alpha = 0.90 > \alpha_c$). The progression from the blue to the green curves (indicated by the red arrow) corresponds to increasing the emergent magnetic field B_{emer} from 0 to 0.25 T with $\gamma_{\text{emer}} = \pi/2$.

the coarse-grained real-space Berry curvature generated by a skyrmion texture. Although \mathbf{B}_{emer} enters the semiclassical equations of motion in the same manner as an external magnetic field \mathbf{B} through $\mathbf{B}_{\text{tot}} = \mathbf{B} + \mathbf{B}_{\text{emer}}$, its role is fundamentally distinct. \mathbf{B}_{emer} encodes real-space topology and couples to the Weyl-node Berry curvature $\Omega_{\mathbf{k}}^x$ via the modified phase-space factor \mathcal{D}^x .

To characterize these behaviors systematically, we adopt the general quadratic fitting form of the magnetoconductivity tensor [22]

$$\sigma_{ij}(B) = \sigma_{ij}^{(0)} + (B - B_0)^2 \sigma_{ij}^{(2)}, \quad (25)$$

which provides a unified framework to describe (i) conventional quadratic-in- B magnetoconductivity, (ii) shifted parabolic behavior, and (iii) complete inversion of the curvature, as schematically illustrated in Fig. 1. Within this parametrization, we define the following three regimes. *Weak-sign-reversal* is characterized by (i)

$B_0 \neq 0$, (ii) $\sigma_{ij}^{(0)} \neq \sigma_{ij}(B = 0)$, and (iii) $\text{sign}(\sigma_{ij}^{(2)}) > 0$. In this case, the vertex of the parabola in $\sigma_{ij}(B)$ shifts away from the origin, and $\sigma_{ij}(B)$ exhibits opposite signs for either small positive or negative magnetic fields. Importantly, the overall curvature remains positive. In the present context, such behavior can arise from the additional real-space topological contribution induced by a finite B_{emer} , which effectively shifts the balance between anomaly-driven enhancement and scattering-induced suppression. *Strong-sign-reversal*, on the other hand, corresponds to $\text{sign}(\sigma_{ij}^{(2)}) < 0$ with $B_0 = 0$, indicating a complete inversion of the parabolic curvature. This regime is typically driven by strong intervalley scattering, which overwhelms the anomaly contribution and reverses the overall magnetic-field response. Finally, when both a curvature inversion ($\text{sign}(\sigma_{ij}^{(2)}) < 0$) and a finite shift ($B_0 \neq 0$) occur simultaneously, the system exhibits a *strong-and-weak sign-reversal* regime. In the mixed-topology scenario considered here, this regime naturally emerges from the cooperative interplay between momentum-space Berry curvature (Weyl monopoles) and real-space topology (skyrmion-induced emergent field). We are now in the position to discuss the magnetoconductivity in the presence of real and momentum space topology.

A. LMC in the presence of real- and momentum-space topology

We begin by recovering the well-established behavior of the LMC in the absence of real-space topology ($B_{\text{emer}} = 0$). Figure 2(a) shows the normalized LMC defined as

$$\frac{\delta\sigma_{zz}(B)}{\sigma_{zz}(0)} = \frac{\sigma_{zz}(B) - \sigma_{zz}(0)}{\sigma_{zz}(0)} \quad (26)$$

for the angle $\gamma = \pi/2$. Increasing the intervalley scattering strength α drives a sign reversal of the LMC across the critical value α_c . For $\alpha < \alpha_c$, the anomaly-induced positive LMC dominates, whereas for $\alpha > \alpha_c$, strong intervalley relaxation overwhelms the chiral pumping mechanism and inverts the curvature of the magnetoconductivity [21, 22, 30–34, 57, 69, 71].

We now incorporate real-space topology through a finite emergent magnetic field \mathbf{B}_{emer} with $\gamma_{\text{emer}} = \pi/2$, representing the coarse-grained Berry curvature generated by a skyrmion texture. The corresponding LMC is shown in Fig. 2(b). Even an infinitesimal B_{emer} qualitatively enriches the magnetic-field dependence of the LMC: the vertex of the parabola shifts away from the origin while its overall curvature remains unchanged for fixed α . According to the classification discussed earlier, this behavior corresponds to *weak sign reversal*. The shift originates from terms linear in B_{emer} that arise through the modified phase-space factor $D_{\mathbf{k}}^X$. Physically, the emergent field modifies the effective magnetic environment experienced by Weyl quasiparticles without altering the intrinsic anomaly mechanism.

Importantly, for a fixed value of B_{emer} , increasing α still leads to inversion of the parabola, i.e., a transition to *strong sign reversal*, as shown in Fig. 2(b). Thus, intervalley scattering controls the curvature of the LMC, while the emergent field controls the shift of its extremum. The coexistence of these two effects naturally gives rise to the *strong-and-weak sign-reversal* regime. To gain further insight, we plot the normalized LMC for two fixed values of α (one below and one above α_c) at different values of B_{emer} in Fig. 3. For $\alpha < \alpha_c$ [Fig. 3(a)], increasing B_{emer} progressively shifts the parabola, producing *weak sign reversal* without changing its positive curvature. In contrast, for $\alpha > \alpha_c$ [Fig. 3(b)], the curvature is already inverted; the addition of B_{emer} introduces an additional shift, leading to the combined *strong-and-weak sign-reversal* regime. These results demonstrate that real-space topology and intervalley scattering affect distinct geometrical features of the LMC curve.

We next analyze the LMC as a function of B_{emer} itself, both in the absence and presence of an external magnetic field, as shown in Figs. 2(c) and 2(d), respectively. In the absence of an external field, the LMC as a function of B_{emer} exhibits a strong sign reversal, reflecting the dominant role of the emergent field in controlling the curvature. When an external magnetic field is present, the interplay between \mathbf{B} and \mathbf{B}_{emer} produces *weak* or *strong-and-weak* sign reversal depending on the value of α . This confirms that B_{emer} acts as an independent topological tuning parameter rather than merely re-normalizing the external magnetic field.

It is important to emphasize that although B_{emer} enters the semiclassical equations of motion through the linear combination $\mathbf{B}_{\text{tot}} = \mathbf{B} + \mathbf{B}_{\text{emer}}$ and has the same sign at both Weyl nodes, its transport effect is not a

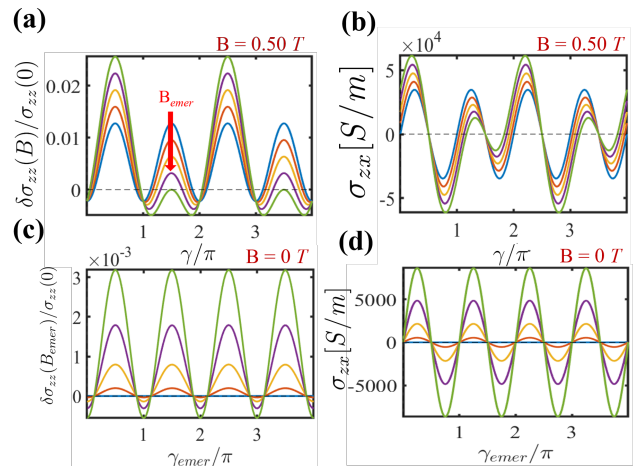


Figure 4. Normalized LMC and PHC for a minimal model of untitled WSM as a function of γ and γ_{emer} . (a) Normalised LMC at $B = 0.5$ T. (b) PHC at $B = 0.5$ T. (c) Normalized LMC for given B_{emer} at $B = 0$ T. (d) PHC for given B_{emer} at $B = 0$ T. In (a)-(d), from blue to green lines, B_{emer} is varied from 0 to 0.25 T with $\gamma = \gamma_{\text{emer}} = \pi/2$.

trivial field renormalization. The key point is that B_{emer} couples to the momentum-space Berry curvature $\Omega_{\mathbf{k}}^X$, which is opposite for opposite chiralities. Consequently, the mixed term $\mathbf{B}_{\text{emer}} \cdot \Omega_{\mathbf{k}}^X$ generates chirality-dependent corrections to the phase-space factor and generalized velocity, thereby modifying the anomaly-driven LMC in a genuinely topological manner. This mixed real- and momentum-space coupling constitutes a central result of the present work.

Finally, we investigate the angular γ -dependence of the normalized LMC in the presence of B_{emer} at $B = 0.5$ T, shown in Fig. 4(a). We observe that the emergent field introduces a pronounced asymmetry in the angular response around $\gamma = \pi$. This asymmetry originates from the fact that B_{emer} has the same sign at both Weyl nodes and therefore breaks the effective inversion symmetry of the magnetotransport response. The resulting angular dependence provides an experimentally accessible signature of the mixed real-space and momentum-space topology. To deepen our understanding of B_{emer} in LMC, we have plotted it as a function of γ_{emer} at different values of B_{emer} in Fig. 4(c) at $B = 0$. The angular anisotropy is clearly visible in this plot. Although the angular dependence remains intact for all values of B_{emer} , the magnitude increases with increasing B_{emer} and the positive portion increases more rapidly than negative one. As discussed earlier, due to the same sign of B_{emer} for both nodes, the fermi surface distorted along the direction of B_{emer} and this leads to an anisotropic response, and shows a maximum LMC for $\mathbf{B}_{\text{emer}} \parallel \hat{z}$.

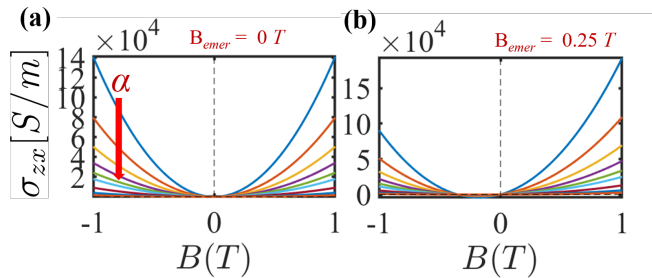


Figure 5. PHC as a function of external magnetic field B for a minimal model of an untilted time-reversal symmetry broken WSM. (a) The emergent magnetic field $B_{\text{emer}} = 0$ T. (b) $B_{\text{emer}} = 0.25$ T. The angle $\gamma = \pi/4$ and $\gamma_{\text{emer}} = \pi/2$. In (a) and (b), α is changed from 0.20 to 1.5 from the top to bottom lines.

B. PHC in the presence of real- and momentum-space topology

Having discussed the LMC, we now turn to PHC. The PHC exhibits a characteristic angular dependence proportional to $\sin(2\gamma)$, where γ is the angle of the applied magnetic field measured from the x -axis [35]. In Fig. 4(b), we plot this angular dependence for different values of B_{emer} . In the presence of B_{emer} , the angular profile becomes asymmetric about $\gamma = \pi$. Although the functional dependence remains similar for $\gamma \in (\pi, 2\pi)$, the magnitude is reduced. This asymmetry arises from the fixed orientation of B_{emer} along the z direction.

To isolate the role of real-space topology, we first evaluate the PHC in the absence of B_{emer} . Figure 5(a) shows the planar Hall conductivity σ_{zx} for several values of the intervalley scattering strength α . In this case, the response is governed purely by momentum-space topology. Increasing α suppresses the magnitude of the PHC; however, unlike the LMC, no sign reversal is observed. When B_{emer} is switched on [Fig. 5(b)], the minima of the PHC parabola shift, but shows weak sign reversal. Fixing α and varying B_{emer} leads to a qualitatively different behavior, shown in Fig. 6(a). In this case, the presence of real-space topology drives the system into a weak-sign-reversal regime. In Fig. 6(b), we plot the PHC as a function of B_{emer} for different values of the external magnetic field. For $B = 0$, the PHC seems to vanish, indicating that an emergent field directed along z alone does not generate a planar Hall response of the same magnitude as the external field does. Increasing the external magnetic field enhances the magnitude of the PHC within the studied parameter range.

To gain further insight, we consider the PHC in the presence of B_{emer} alone while varying its direction within the xz -plane, as shown in Fig. 4(d). Which shows PHC has very less magnitude, but still finite. It also confirm that B_{emer} can alone give a finite PHC. It is clear that $\sigma_{zx} \propto \sin 2\gamma_{\text{emer}}$, which is intact for all finite values of B_{emer} taken. This has never been explored before.

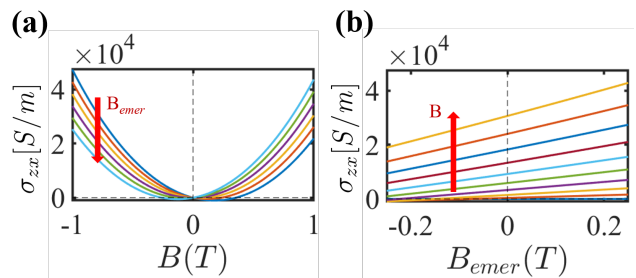


Figure 6. PHC for a minimal model of an untilted time-reversal symmetry broken WSM. (a) PHC as a function of the external magnetic field B . Along the red arrow, the emergent magnetic field B_{emer} changes from -0.25 T to 0.25 T. (b) PHC as a function of B_{emer} . Along the red arrow, B changes from 0 to 1 T. In both, $\gamma = \pi/4$, $\gamma_{\text{emer}} = \pi/2$, and $\alpha < \alpha_c$.

V. CONCLUSIONS

We have investigated magnetotransport in a time-reversal symmetry–broken, untilted WSM in the simultaneous presence of momentum-space Berry curvature and real-space topology encoded through an emergent magnetic field \mathbf{B}_{emer} . Within a semiclassical Boltzmann framework, we systematically analyzed the LMC and PHC in this mixed-topology setting. In the absence of real-space topology, we recover the known behavior: the LMC undergoes a strong sign reversal as intervalley scattering increases beyond a critical value, reflecting the competition between anomaly-driven charge pumping and relaxation. Upon introducing a finite B_{emer} , the magnetoconductivity acquires an additional shift of its parabolic profile, corresponding to a weak-sign-reversal regime. While intervalley scattering controls the curvature of the response, the emergent field controls the shift of its extremum. Their combined action naturally generates a strong-and-weak sign-reversal regime, demonstrating that real- and momentum-space topology affect distinct geometrical features of the magnetoconductivity.

We further showed that the emergent field induces a pronounced asymmetry in the angular dependence of both longitudinal and planar Hall conductivities. For the planar Hall response, \mathbf{B}_{emer} modifies the magnitude and can drive weak-sign-reversal behavior, while preserving the characteristic $\sin(2\gamma)$ dependence. Notably, a finite PHC can arise solely from \mathbf{B}_{emer} when its direction is varied, confirming that real-space topology alone can generate a measurable transverse response. Our results establish that \mathbf{B}_{emer} does not merely re-normalize the external magnetic field through $\mathbf{B}_{\text{tot}} = \mathbf{B} + \mathbf{B}_{\text{emer}}$. Instead, through its coupling to momentum-space Berry curvature, it acts as an independent topological tuning parameter. The interplay between Weyl monopoles and skyrmion-induced emergent fields provides a direct transport signature of mixed real- and momentum-space

topology.

Our results suggest clear experimental signatures that can be probed using angle-dependent magnetotransport measurements in magnetic Weyl semimetals hosting nontrivial spin textures. By rotating the external magnetic field within the transport plane, one can measure the LMC and PHC as functions of both the field magnitude and orientation. The interplay between Berry curvature in momentum space and the emergent magnetic field generated by real-space topology is predicted to produce two distinct features: (i) a finite shift of the magnetoconductivity parabola away from $B = 0$, and (ii) an angular asymmetry of the magnetotransport response about $\gamma = \pi$. Since the emergent field is directly related to the density of magnetic textures, these transport signatures should evolve with the skyrmion density, which can be independently characterized using magnetic imaging techniques such as Lorentz transmission electron microscopy or magnetic force microscopy. Observation of these features would provide direct experimental evidence of mixed real- and momentum-space topology in Weyl systems.

VI. ACKNOWLEDGMENTS

The authors are grateful to Amit Agarwal and Gargee Sharma for their insightful discussions and valuable scientific input. A.A. acknowledges financial support from project: SPO/ANRF/PHY/2024434 and IIT Mandi for providing computing facilities. TT acknowledges financial support by the Japan Society for the Promotion of Science, KAKENHI (Grants No. 25H01248) from the Ministry of Education, Culture, Sports, Science, and Technology, Japan.

Appendix A: Real and momentum space mixed term in the current

We evaluate the current solely from the nonequilibrium correction, which is first order in E :

$$\mathbf{J} = -e \sum_{\chi, \mathbf{k}} \mathbf{v}_0^\chi g_{\mathbf{k}}^{1, \chi}. \quad (\text{A1})$$

Using $\mathbf{v}_0^\chi = \mathcal{D}^\chi [\mathbf{v}_{\mathbf{k}}^\chi + \frac{e}{\hbar} (\mathbf{v}_{\mathbf{k}}^\chi \cdot \boldsymbol{\Omega}^\chi) \mathbf{B}_{\text{tot}}]$, the weak-field expansion gives $\mathbf{v}_0^\chi \simeq \mathbf{v}_{\mathbf{k}}^\chi + \frac{e}{\hbar} (\mathbf{v}_{\mathbf{k}}^\chi \cdot \boldsymbol{\Omega}^\chi) \mathbf{B}_{\text{tot}} - \frac{e}{\hbar} (\mathbf{B}_{\text{tot}} \cdot \boldsymbol{\Omega}^\chi) \mathbf{v}_{\mathbf{k}}^\chi$. In constant relaxation-time approximation, $g_{\mathbf{k}}^{1, \chi} = -e\tau \mathbf{E} \cdot \mathbf{v}_{\mathbf{k}}^\chi \left(-\frac{\partial f_0}{\partial \epsilon}\right)$. Keeping only terms linear in \mathbf{B}_{emer} , we obtain

$$\begin{aligned} \mathbf{J}_{\text{cross}} &= \frac{e^3 \tau}{\hbar} \sum_{\chi, \mathbf{k}} \left(-\frac{\partial f_0}{\partial \epsilon}\right) (\mathbf{E} \cdot \mathbf{v}_{\mathbf{k}}^\chi) \\ &\quad \times [(\mathbf{v}_{\mathbf{k}}^\chi \cdot \boldsymbol{\Omega}^\chi) \mathbf{B}_{\text{emer}} - (\mathbf{B}_{\text{emer}} \cdot \boldsymbol{\Omega}^\chi) \mathbf{v}_{\mathbf{k}}^\chi]. \end{aligned} \quad (\text{A2})$$

For longitudinal transport, $\mathbf{E} = E_z \hat{z}$ and $\mathbf{B}_{\text{emer}} = B_{\text{emer}} \hat{z}$. Then

$$\begin{aligned} J_z^{\text{cross}} &= \frac{e^3 \tau E_z B_{\text{emer}}}{\hbar} \\ &\quad \times \sum_{\chi, \mathbf{k}} \left(-\frac{\partial f_0}{\partial \epsilon}\right) v_{k,z}^\chi [(\mathbf{v}_{\mathbf{k}}^\chi \cdot \boldsymbol{\Omega}^\chi) - \Omega_z^\chi v_{k,z}^\chi]. \end{aligned} \quad (\text{A3})$$

Thus the longitudinal conductivity acquires a term

$$\sigma_{zz}^{\text{cross}} \propto B B_{\text{emer}}, \quad (\text{A4})$$

which is linear in B_{emer} and linear in B (through the standard anomaly correction inside g^1 when solved self-consistently). Including the usual anomaly contribution $\propto B^2$, the conductivity takes the form

$$\sigma_{zz}(B) = \sigma_{zz}^{(0)} + a_1 \left(B + \frac{b_1}{2a_1} B_{\text{emer}}\right)^2 - \frac{b_1^2}{4a_1} B_{\text{emer}}^2. \quad (\text{A5})$$

Hence the extremum shifts to

$$B_0 = -\frac{b_1}{2a_1} B_{\text{emer}}. \quad (\text{A6})$$

For $\mathbf{B} = B(\cos \gamma \hat{x} + \sin \gamma \hat{z})$ and $\mathbf{B}_{\text{emer}} = B_{\text{emer}} \hat{z}$, the mixed term in Eq. (A2) produces contributions proportional to $B B_{\text{emer}} \sin \gamma$, which are not invariant under $\gamma \rightarrow \gamma + \pi$. Therefore, $\sigma(\gamma) \neq \sigma(\gamma + \pi)$, leading to angular asymmetry induced purely by the real-momentum space cross coupling. Physically, since B_{emer} has the same sign at both Weyl nodes while $\boldsymbol{\Omega}^\chi$ changes sign with chirality, the mixed term remains chirality dependent and breaks the effective inversion symmetry of the angular magnetotransport response.

- [1] D. K. Le, E. Thareja, B. Konushbaev, G. Pantano, T. Saunderson, M.-H. Phan, Y. Mokrousov, and J. Gayles, Ultra-stable weyl topology driven by magnetic textures in the shandite compound $\text{Co}_3\text{Sn}_2\text{S}_6$ (2-x) Se_x , arXiv preprint arXiv:2601.09922 (2026).
- [2] L. Dominici, A. Rahmani, D. Colas, D. Ballarini, M. De Giorgi, G. Gigli, D. Sanvitto, F. P. Laussy, and N. Voronova, Coupled quantum vortex kinematics and berry curvature in real space, *Communications Physics* **6**, 197 (2023).
- [3] B. He, M. Yao, Y. Pan, K. E. Arpino, D. Chen, F. M. Serrano-Sanchez, S. Ju, M. Shi, Y. Sun, and C. Felser, Enhanced weyl semimetal signature in $\text{Co}_3\text{Sn}_2\text{S}_6$ kagome ferromagnet by chlorine doping, *Communications Materials* **5**, 275 (2024).
- [4] M. Raju, R. Romero III, D. Nishio-Hamane, R. Uesugi, M. Asakura, Z. Tagay, T. Higo, N. Armitage, C. Broholm, and S. Nakatsuji, Anisotropic anomalous transport in the kagome-based topological antiferromagnetic Mn_3Ga epitaxial thin films, *Physical Review Materials* **8**, 014204 (2024).
- [5] X. Wan, A. M. Turner, A. Vishwanath, and S. Y. Savrasov, Topological semimetal and fermi-arc surface states in the electronic structure of pyrochlore iridates, *Physical Review B* **83**, 205101 (2011).
- [6] N. Armitage, E. Mele, and A. Vishwanath, Weyl and dirac semimetals in three-dimensional solids, *Reviews of Modern Physics* **90**, 015001 (2018).
- [7] D. T. Son and N. Yamamoto, Berry curvature, triangle anomalies, and the chiral magnetic effect in fermi liquids, *Physical review letters* **109**, 181602 (2012).
- [8] A. Burkov, Anomalous hall effect in weyl metals, *Physical Review Letters* **113**, 187202 (2014).
- [9] M. V. Berry, Quantal phase factors accompanying adiabatic changes, *Proceedings of the Royal Society of London. A. Mathematical and Physical Sciences* **392**, 45 (1984).
- [10] G. Sundaram and Q. Niu, Wave-packet dynamics in slowly perturbed crystals: Gradient corrections and berry-phase effects, *Physical Review B* **59**, 14915 (1999).
- [11] D. Xiao, M.-C. Chang, and Q. Niu, Berry phase effects on electronic properties, *Reviews of modern physics* **82**, 1959 (2010).
- [12] N. Nagaosa and Y. Tokura, Topological properties and dynamics of magnetic skyrmions, *Nature nanotechnology* **8**, 899 (2013).
- [13] N. Verma, Z. Addison, and M. Randeria, Unified theory of the anomalous and topological hall effects with phase-space berry curvatures, *Science Advances* **8**, eabq2765 (2022).
- [14] P. Goswami and S. Tewari, Axionic field theory of (3+1)-dimensional weyl semimetals, *Physical Review B* **88**, 245107 (2013).
- [15] M. Hirschberger, T. Nakaajima, S. Gao, L. Peng, A. Kikkawa, T. Kurumaji, M. Kriener, Y. Yamasaki, H. Sagayama, H. Nakao, *et al.*, Skyrmion phase and competing magnetic orders on a breathing kagomé lattice, *Nature communications* **10**, 5831 (2019).
- [16] M. Hirschberger, B. G. Szigeti, M. Hemmida, M. M. Hirschmann, S. Esser, H. Ohsumi, Y. Tanaka, L. Spitz, S. Gao, K. K. Kolincio, *et al.*, Lattice-commensurate skyrmion texture in a centrosymmetric breathing kagome magnet, *npj Quantum Materials* **9**, 45 (2024).
- [17] Q. Du, M.-G. Han, Y. Liu, W. Ren, Y. Zhu, and C. Petrovic, Room-temperature skyrmion thermopower in Fe_3Sn_2 , *Advanced Quantum Technologies* **3**, 2000058 (2020).
- [18] P. Vir, J. Gayles, A. Sukhanov, N. Kumar, F. Damay, Y. Sun, J. Kübler, C. Shekhar, and C. Felser, Anisotropic topological hall effect with real and momentum space berry curvature in the antiskyrmion-hosting heusler compound Mn_2Si , *Physical Review B* **99**, 140406 (2019).
- [19] Z. Addison, L. Keyes, and M. Randeria, Anomalous and topological hall effects with phase-space berry curvatures: Electric, thermal, and thermoelectric transport in magnets, *Physical Review B* **112**, 014446 (2025).
- [20] B. Göbel, L. Schimpf, and I. Mertig, Topological orbital hall effect caused by skyrmions and antiferromagnetic skyrmions, *Communications Physics* **8**, 17 (2025).
- [21] A. Ahmad and G. Sharma, Longitudinal magnetoconductance and the planar hall effect in a lattice model of tilted weyl fermions, *Physical Review B* **103**, 115146 (2021).
- [22] A. Ahmad, K. V. Raman, S. Tewari, and G. Sharma, Longitudinal magnetoconductance and the planar hall conductance in inhomogeneous weyl semimetals, *Physical Review B* **107**, 144206 (2023).
- [23] G. Volovik, On induced cpt-odd chern-simons terms in the 3+1 effective action, *Journal of Experimental and Theoretical Physics Letters* **70**, 1 (1999).
- [24] C.-X. Liu, P. Ye, and X.-L. Qi, Chiral gauge field and axial anomaly in a weyl semimetal, *Physical Review B* **87**, 235306 (2013).
- [25] A. G. Grushin, Consequences of a condensed matter realization of lorentz-violating qed in weyl semi-metals, *Physical Review D* **86**, 045001 (2012).
- [26] A. Zyuzin and A. Burkov, Topological response in weyl semimetals and the chiral anomaly, *Physical Review B* **86**, 115133 (2012).
- [27] B. Yan and C. Felser, Topological materials: Weyl semimetals, *Annual Review of Condensed Matter Physics* **8**, 337 (2017).
- [28] B. Lv, H. Weng, B. Fu, X. P. Wang, H. Miao, J. Ma, P. Richard, X. Huang, L. Zhao, G. Chen, *et al.*, Experimental discovery of weyl semimetal TaAs , *Physical Review X* **5**, 031013 (2015).
- [29] M. Z. Hasan, G. Chang, I. Belopolski, G. Bian, S.-Y. Xu, and J.-X. Yin, Weyl, dirac and high-fold chiral fermions in topological quantum matter, *Nature Reviews Materials* **6**, 784 (2021).
- [30] A. Ahmad, G. Varma, and G. Sharma, Geometry, anomaly, topology, and transport in weyl fermions, *Journal of Physics: Condensed Matter* **37**, 043001 (2024).
- [31] G. Sharma, S. Nandy, and S. Tewari, Sign of longitudinal magnetoconductivity and the planar hall effect in weyl semimetals, *Physical Review B* **102**, 205107 (2020).
- [32] G. Varma, M. H. Raza, and A. Ahmad, Chiral anomaly-induced nonlinear hall effect in spin-orbit coupled noncentrosymmetric metals, *Physical Review B* **113**, 035112 (2026).

- [33] A. Ahmad and G. Sharma, Longitudinal magnetoconductance of higher-pseudospin fermions, *Physical Review B* **112**, 045135 (2025).
- [34] A. Ahmad, G. V. K, and G. Sharma, Chiral anomaly induced nonlinear hall effect in three-dimensional chiral fermions, *Physical Review B* **111**, 035138 (2025).
- [35] S. Nandy, G. Sharma, A. Taraphder, and S. Tewari, Chiral anomaly as the origin of the planar hall effect in weyl semimetals, *Physical review letters* **119**, 176804 (2017).
- [36] S. Nandy, C. Zeng, and S. Tewari, Chiral anomaly induced nonlinear hall effect in semimetals with multiple weyl points, *Physical Review B* **104**, 205124 (2021).
- [37] S.-B. Zhang, H.-Z. Lu, and S.-Q. Shen, Linear magnetoconductivity in an intrinsic topological weyl semimetal, *New Journal of Physics* **18**, 053039 (2016).
- [38] S. A. Yang, H. Pan, and F. Zhang, Chirality-dependent hall effect in weyl semimetals, *Physical review letters* **115**, 156603 (2015).
- [39] S. Nandy, C. Zeng, and S. Tewari, Chiral anomaly induced nonlinear hall effect in semimetals with multiple weyl points, *Phys. Rev. B* **104**, 205124 (2021).
- [40] K. Das and A. Agarwal, Berry curvature induced thermopower in type-i and type-ii weyl semimetals, *Physical Review B* **100**, 085406 (2019).
- [41] K. Das, S. K. Singh, and A. Agarwal, Chiral anomalies induced transport in weyl metals in quantizing magnetic field, *Physical Review Research* **2**, 033511 (2020).
- [42] S. Das, K. Das, and A. Agarwal, Nonlinear magnetoconductivity in weyl and multi-weyl semimetals in quantizing magnetic field, *Physical Review B* **105**, 235408 (2022).
- [43] G. Sharma and S. Tewari, Transverse thermopower in dirac and weyl semimetals, *Physical Review B* **100**, 195113 (2019).
- [44] G. Sharma, P. Goswami, and S. Tewari, Nernst and magnetothermal conductivity in a lattice model of weyl fermions, *Physical Review B* **93**, 035116 (2016).
- [45] G. Sharma, P. Goswami, and S. Tewari, Chiral anomaly and longitudinal magnetotransport in type-ii weyl semimetals, *Physical Review B* **96**, 045112 (2017).
- [46] C. Zeng, S. Nandy, and S. Tewari, Nonlinear transport in weyl semimetals induced by berry curvature dipole, *Physical Review B* **103**, 245119 (2021).
- [47] G. Sharma, C. Moore, S. Saha, and S. Tewari, Nernst effect in dirac and inversion-asymmetric weyl semimetals, *Physical Review B* **96**, 195119 (2017).
- [48] S. Nandy, A. Taraphder, and S. Tewari, Planar thermal hall effect in weyl semimetals, *Physical Review B* **100**, 115139 (2019).
- [49] K. Das and A. Agarwal, Thermal and gravitational chiral anomaly induced magneto-transport in weyl semimetals, *Physical Review Research* **2**, 013088 (2020).
- [50] S. Das, K. Das, and A. Agarwal, Chiral anomalies in three-dimensional spin-orbit coupled metals: Electrical, thermal, and gravitational anomalies, *Physical Review B* **108**, 045405 (2023).
- [51] D. Mandal, K. Das, and A. Agarwal, Chiral anomaly and nonlinear magnetotransport in time reversal symmetric weyl semimetals, *Physical Review B* **106**, 035423 (2022).
- [52] I. Mandal and K. Saha, Thermopower in an anisotropic two-dimensional weyl semimetal, *Physical Review B* **101**, 045101 (2020).
- [53] I. Mandal and A. Sen, Tunneling of multi-weyl semimetals through a potential barrier under the influence of magnetic fields, *Physics Letters A* **399**, 127293 (2021).
- [54] R. Ghosh, F. Haidar, and I. Mandal, Linear response in planar hall and thermal hall setups for rarita-schwinger-weyl semimetals, *Physical Review B* **110**, 245113 (2024).
- [55] T. Schulz, R. Ritz, A. Bauer, M. Halder, M. Wagner, C. Franz, C. Pfleiderer, K. Everschor, M. Garst, and A. Rosch, Emergent electrodynamics of skyrmions in a chiral magnet, *Nature Physics* **8**, 301 (2012).
- [56] K.-S. Kim, H.-J. Kim, and M. Sasaki, Boltzmann equation approach to anomalous transport in a weyl metal, *Physical Review B* **89**, 195137 (2014).
- [57] A. Knoll, C. Timm, and T. Meng, Negative longitudinal magnetoconductance at weak fields in weyl semimetals, *Physical Review B* **101**, 201402 (2020).
- [58] M. Imran and S. Hershfield, Berry curvature force and lorentz force comparison in the magnetotransport of weyl semimetals, *Physical Review B* **98**, 205139 (2018).
- [59] V. A. Zyuzin, Magnetotransport of weyl semimetals due to the chiral anomaly, *Physical Review B* **95**, 245128 (2017).
- [60] K. Das and A. Agarwal, Linear magnetochiral transport in tilted type-i and type-ii weyl semimetals, *Physical Review B* **99**, 085405 (2019).
- [61] C. Duval, Z. Horváth, P. A. Horvathy, L. Martina, and P. Stichel, Comment on “berry phase correction to electron ρ density of states in solids”, *Physical Review Letters* **96**, 099701 (2006).
- [62] G. D. Mahan, *9. Many-Particle Systems* (Princeton University Press, 2008).
- [63] H. Bruus and K. Flensberg, *Many-body quantum theory in condensed matter physics: an introduction* (Oxford university press, 2004).
- [64] J. M. Ziman, *Principles of the Theory of Solids* (Cambridge university press, 1979).
- [65] E. Abers, *Quantum Mechanics* (Pearson Education, 2004).
- [66] T. Morimoto, S. Zhong, J. Orenstein, and J. E. Moore, Semiclassical theory of nonlinear magneto-optical responses with applications to topological dirac/weyl semimetals, *Physical Review B* **94**, 245121 (2016).
- [67] I. Sodemann and L. Fu, Quantum nonlinear hall effect induced by berry curvature dipole in time-reversal invariant materials, *Physical review letters* **115**, 216806 (2015).
- [68] D. Son and B. Spivak, Chiral anomaly and classical negative magnetoresistance of weyl metals, *Physical Review B* **88**, 104412 (2013).
- [69] G. Varma K, A. Ahmad, S. Tewari, and G. Sharma, Magnetotransport in spin-orbit coupled noncentrosymmetric and weyl metals, *Physical Review B* **109**, 165114 (2024).
- [70] G. Sharma, S. Nandy, K. V. Raman, and S. Tewari, Decoupling intranode and internode scattering in weyl fermions, *Physical Review B* **107**, 115161 (2023).
- [71] G. Varma K, A. Ahmad, and G. Sharma, Strain-induced ettingshausen effect in spin-orbit coupled noncentrosymmetric metals, *Physical Review B* **113**, 075118 (2026).